Investigations of nano-crystalline Sr0.5Ba0.5Nb2O6 and bulk ceramics synthesized by a polymerization method using PEG400

Roberto Köferstein, Florian Oehler, Stefan G Ebbinghaus

J. Eur. Ceram. Soc. 39 (2019) 1156-1163

DOI: 10.1016/j.jeurceramsoc.2018.11.043

https://doi.org/10.1016/j.jeurceramsoc.2018.11.043

Investigations of nano-crystalline $Sr_{0.5}Ba_{0.5}Nb_2O_6$ and bulk ceramics synthesized by a polymerization method using PEG400

Roberto Köferstein*, Florian Oehler, and Stefan G. Ebbinghaus

Institute of Chemistry, Martin Luther University Halle-Wittenberg,

Kurt-Mothes-Straße 2, 06120 Halle, Germany.

* Corresponding author. Tel.: +49-345-5525630; Fax: +49-345-5527028.

E-mail address: roberto.koeferstein@chemie.uni-halle.de

Abstract. Nano-crystalline $Sr_{0.5}Ba_{0.5}Nb_2O_6$ was synthesized by a one-pot method using PEG400 and citric acid. Calcination of the (Sr,Ba,Nb)-gel at 600 °C leads to $Sr_{0.5}Ba_{0.5}Nb_2O_6$ with a crystallite size of 24(2) nm and a specific surface area of 38.5(10) $m^2 g^{-1}$. Sintering up to 1325 °C leads to ceramics with globular or irregular-shaped grains and average grain sizes between 1.3 and 2.4 µm, whereas higher temperatures lead to a rod-like microstructure. The indirect allowed optical band gap varies between 3.70(5) and 3.29(5) eV. Dielectric measurements show a diffuse phase transition and weak relaxor properties. The maximum of the permittivity occurs between 116 and 147 °C. The frequency dependence of the impedance can be well described by one or two RC-circuits depending on sintering temperature. The

melting temperature is determined as 1506(7) °C with ΔH_f = 140(20) kJ mol^{-1}. The average linear thermal expansion coefficient is found to be 10.5(5)·10^{-6} K^{-1}.

Keywords: *tungsten bronze; strontium barium niobate; dielectric permittivity; nano-particle; band-gap*

1. Introduction

Strontium barium niobate ($Sr_xBa_{1-x}Nb_2O_6$, SBN) is of interest for applications in advanced technologies because of its electro-optic, piezoelectric, pyroelectric, ferroelectric and photorefractive properties [1–6]. In addition, $Sr_xBa_{1-x}Nb_2O_6$ can be also used as photocatalyst for water splitting [7–9]. $Sr_xBa_{1-x}Nb_2O_6$ is a lead-free relaxor ferroelectric which exists in the range of $0.25 \leq x \leq 0.75$ [10] and crystallizes in the tetragonal tungsten-bronze (TTB) structure [10,11]. The relaxor behaviour increases with the strontium content [6,12]. The temperature of the permittivity maximum (T_m), which represents the transition from the ferroelectric to the paraelectric state, depends strongly on the composition [6,10]. Reported T_m values for single crystals of $Sr_{0.5}Ba_{0.5}Nb_2O_6$ are between 110 and 130 °C [6,10,13], whereas for polycrystalline ceramics prepared by the conventional mixed-oxide method T_m vary from 74 to 177 °C [14–16]. Interestingly, dielectric measurements on $Sr_{0.5}Ba_{0.5}Nb_2O_6$ ceramics prepared by wet-chemical syntheses reveal lower T_m values by trend typically between 40 and 119 °C [17–20]. Patro et al. [21] reported on a permittivity maximum even at –49 °C for $Sr_{0.5}Ba_{0.5}Nb_2O_6$ ceramics prepared by a combustion synthesis using glycine as fuel.

Polycrystalline $Sr_{0.5}Ba_{0.5}Nb_2O_6$ samples are usually synthesized by the conventional mixed-oxide method which requires high calcining temperatures and results in coarse-grained ceramic bodies [22–26]. In the last years, a few soft-chemical synthesis routes have been

reported, such as co-precipitation [17,18,27], sol-gel [19,20,28–30], combustion [21,31] and complex precursor [32] routes. Soft-chemistry syntheses enable to synthesize nano-sized powders at low reaction temperatures. Using nano-sized powders ceramics with fine-grained and tunable microstructures can be obtained.

In this paper we report on a polymerization method using PEG400 and citric acid to synthesize nano-crystalline $Sr_{0.5}Ba_{0.5}Nb_2O_6$ powders at low temperatures and ceramics obtained from these powders. Phase evolution and crystallite growth during calcination and sintering were monitored by XRD. The microstructure and sintering properties of the ceramic bodies were studied. Furthermore, the samples were characterized by dielectric and diffuse reflectance measurements. Finally, we determined the melting point, enthalpy of fusion, and the linear thermal expansion coefficient of $Sr_{0.5}Ba_{0.5}Nb_2O_6$ ceramics.

2. Experimental

2.1. Material preparation

$NbCl_5$ (0.007 mol, Alfa Aesar, 99 %) was dissolved in 10 ml 2-methoxyethanol. After addition of 30 ml polyethylene glycol (PEG400) and 20 g citric acid the mixture was stirred on a heating plate at 150 °C until it became a clear solution. $SrCl_2 \cdot 6H_2O$ and $BaCl_2 \cdot 2H_2O$ (0.00175 mol) were dissolved in 5 ml 1,2-ethanediol and added to the above hot Nb-solution. The temperature of the heating plate was increased to 180 °C until the resulting solution turned to a white turbid suspension. Afterwards, the reaction mixture was continuously stirred on the heating plate at 250 °C to obtain a white viscous gel. This (Sr,Ba,Nb)-gel was calcined for 2 h in static air at various temperatures leading to $Sr_{0.5}Ba_{0.5}Nb_2O_6$ nano powders.

Ceramic bodies were obtained using a $Sr_{0.5}Ba_{0.5}Nb_2O_6$ powder calcined at 600 °C for 2 h, mixed with 5 wt.% of a saturated aqueous polyvinyl alcohol (PVA) solution as a pressing aid and uniaxially pressed at about 100 MPa into pellets (green density 2.1 g cm^{-3}). These pellets were placed on a ZrO_2 fibre mat and sintered to ceramic bodies.

For comparative purposes, $Sr_{0.5}Ba_{0.5}Nb_2O_6$ was also prepared via the conventional mixed-oxide method. Stoichiometric amounts of $SrCO_3$, $BaCO_3$ (Merck, extra pure), and Nb_2O_5 (Fluka, puriss. >99.9 %) were well milled together using ZrO_2-balls in propan-2-ol. After filtering and drying the mixture was calcined at 1150 °C for 2 h and afterwards at 1200 °C for 5 h yielding phase-pure $Sr_{0.5}Ba_{0.5}Nb_2O_6$ powder.

2.2. Characterization

X-ray powder diffraction patterns were recorded at room temperature on a *Bruker D8-Advance* diffractometer, equipped with a one-dimensional silicon strip detector (LynxEye™) using Cu-K_α radiation. Crystallite size and the strain parameter were calculated from XRD line broadening (integral peak breadth) using the Scherrer and Wilson equation (pattern fitting by software suite WinXPOW [33]). The full pattern refinement software PowderCell 2.4 [34] was used to determine the amorphous content of the powder samples. Lattice parameters were calculated with the Rietveld software FullProf [35]. Dilatometric measurements were carried out in flowing synthetic air (50 ml min^{-1}) in a *Setaram* TMA 92-16.18 dilatometer. Thermogravimetric (TG) and differential thermoanalytic (DSC) investigations in flowing synthetic air or nitrogen (50 ml min^{-1}) were performed using a *Netzsch* STA 449 system. The TG/DSC measurement of the decomposition of the (Sr,Ba,Nb)-gel was carried out on a sample preheated at 300 °C. The specific surface area (BET) was determined using nitrogen five-point gasphysisorption (Nova 1000, Quantachrome Corporation). The equivalent BET particle diameter was calculated assuming a spherical or cubic particle shape. Scanning electron microscope images were recorded with a *Phenom* ProX SEM in the backscattered electron mode (BSE). An Impedance Analyzer 4192A (Hewlett Packard) was used for frequency- and temperature dependent impedance measurements. Gold electrodes were sputtered onto the ceramic bodies in a *Cressington* Sputter Coater 108auto. Diffuse

reflectance spectra were recorded at room temperature using a *Perkin Elmer* UV–Vis spectrometer Lambda 19 with $BaSO_4$ as white standard.

3. Results and discussion

3.1. Synthesis and powder characterization

Heating of the viscous (Sr,Ba,Nb)-gel in static air at 300 °C for 0.5 h resulted in a black-brown amorphous powder. Simultaneous TG/DSC measurements up to 1000 °C (heating rate 10 K min^{-1}) in flowing air were carried out on this powder (Fig. 1). The decomposition starts at 160 °C and is accompanied by several broad exothermic signals. A strong exothermic reaction with an onset temperature of 444 °C results in a total weight loss of 94 % until 513 °C. Up to 1000 °C no further weight change can be observed. The white residue was identified as $Sr_{0.5}Ba_{0.5}Nb_2O_6$ by XRD measurement.

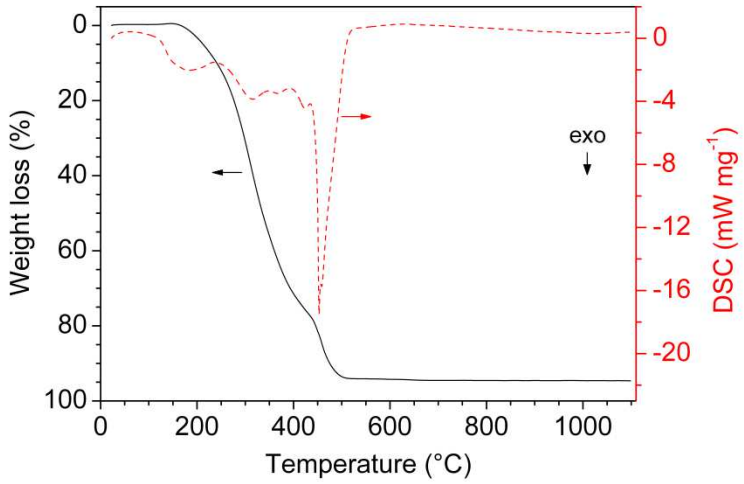

Fig. 1: TG–DSC measurements of a pre-heated (Sr,Ba,Nb)-gel in flowing air (heating rate 10 K min^{-1}).

Fig. 2 shows the phase evolution after thermal decomposition of the (Sr,Ba,Nb)-gel in a muffle furnace in static air (heating rate 10 K min^{-1}, soaking time 2 h). Calcining at 500 °C results in a white amorphous sample (Graph 2a). The weak peak at $2\theta = 28.4°$ indicates small

amounts of crystalline Nb_2O_5 (JCPDS #00-030-873). After calcination at 600 °C (Graph 2b) the white powder shows only reflections of $Sr_{0.5}Ba_{0.5}Nb_2O_6$ (JCPDS #01-074-6520). However, the increased background level at lower diffraction angles, primarily in the range 2θ = 20–30°, suggests the presence of an amorphous fraction. This amorphous content was determined by XRD to be about 25–30 wt.% using the common internal standard method and full pattern refinement [36–38]. With rising calcination temperature the amorphous phase decreased and heating at 1000 °C (Graph 2c) leads to well pronounced $Sr_{0.5}Ba_{0.5}Nb_2O_6$ reflections, however closer inspection shows a very weak shoulder at about 2θ = 29.1°, which is caused by a trace amount of $Ba_3Sr_2Nb_4O_{15}$ or $Sr_3Ba_2Nb_4O_{15}$ (JCPDS #00-058-0642; #00-056-0406). Calcining at 1100 °C results in single-phase $Sr_{0.5}Ba_{0.5}Nb_2O_6$ (Graph 2d). The volume-weighted average crystallite size of the crystalline $Sr_{0.5}Ba_{0.5}Nb_2O_6$ phase increases from 24(2) to 39(3), 69(7), 102(14), and 121(11) nm after calcination at 600, 800, 1000, 1100, and 1200 °C for 2 h.

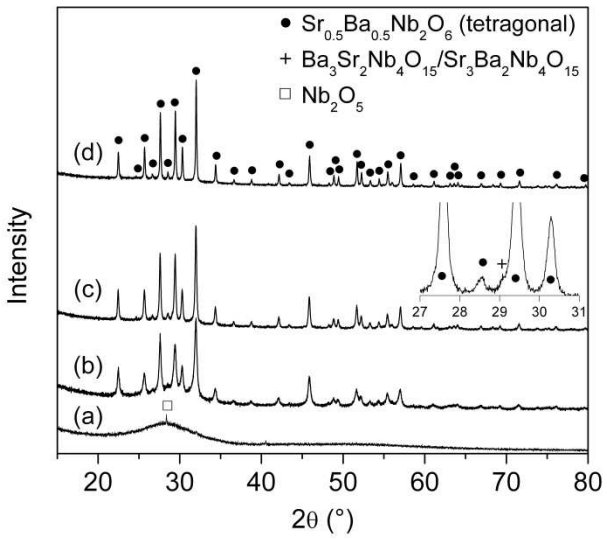

Fig. 2: Room temperature XRD patterns of the (Sr,Ba,Nb)-gel after calcination at various temperatures for 2 h: (a) 500 °C, (b) 600 °C, (c) 1000 °C , and 1100 °C (heating rate 10 K min^{-1}). The inset shows a magnification of graph (c).

The presented synthesis route using PEG400 led to a significant reduction of the reaction temperature to 600 °C for $Sr_{0.5}Ba_{0.5}Nb_2O_6$, compared to conventional and other wet-chemical syntheses [20,21,22] which need at least 700 °C. The formation of $Sr_{0.5}Ba_{0.5}Nb_2O_6$ together with an amorphous fraction at low temperature can often be seen using wet-chemical methods [21,30,32,39]. Recently, Chen et al. [19] prepared $Sr_{0.5}Ba_{0.5}Nb_2O_6$ by a sol-gel synthesis using 1,2-ethanediol and citric acid as polymerization agents. Calcination of that gel resulted in considerable amounts of secondary phases up to 1100 °C.

3.2. Sintering behavior and microstructure of ceramic bodies

Prior to the investigation of the sintering behavior and preparation of ceramic bodies, the (Sr,Ba,Nb)-gel was calcined at 600 °C for 2 h. As mentioned above, this thermal treatment leads to a white $Sr_{0.5}Ba_{0.5}Nb_2O_6$ powder with a small amount of an amorphous fraction. The volume-weighted average crystallite size of the nano-crystalline $Sr_{0.5}Ba_{0.5}Nb_2O_6$ phase was calculated to be 24(2) nm and the root-mean square strain is 0.0012(3). The specific surface area of that powder was determined as 38.5(10) $m^2\ g^{-1}$ corresponding to an equivalent particle size of 29(2) nm, which agrees well with the crystallite size. The nano-crystalline powder was pressed to pellets and isothermally sintered for 10 h in static air at different temperatures (heating-/ cooling rate: 5 K min^{-1}). The final bulk densities (Fig. 3) of the ceramic bodies were calculated from their weight and geometric dimensions and the relative bulk densities are related to the single crystal density of 5.37 g cm^{-3} (ICSD #291175 [25]).

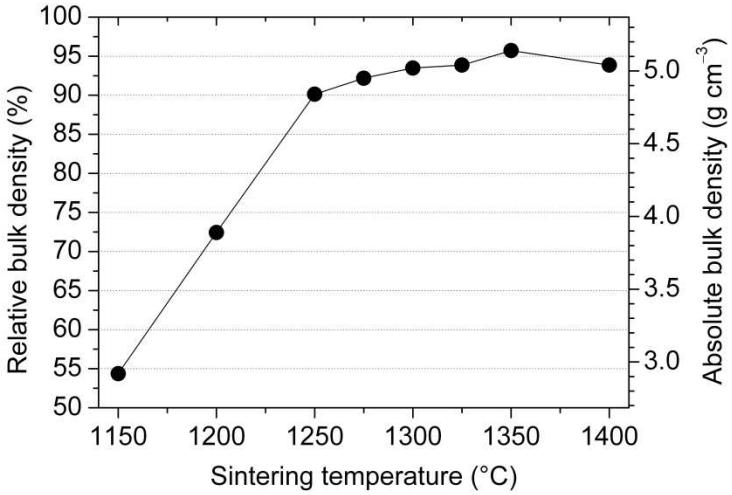

Fig. 3: Final bulk densities of ceramic bodies depending on sintering temperature (rate 5 K min^{-1}, soaking time 10 h). The uncertainty of the data is smaller than the symbol size and is about 0.07 g/cm^3.

Sintering at 1150 °C and 1200 °C leads to an insufficient densification with relative densities of 54(1) and 74(1) %, respectively. Dense ceramics (relative density ≥ 90 %) can be obtained after sintering at 1250 °C. Sintering at 1300 °C results in a relative density of 93(1) % which rises to 96(1) % at 1350 °C. The density drops down to 94(1) % after sintering at 1400 °C caused by the formation of small cracks inside the ceramic body. The typical microstructures and grain sizes of selected ceramics are shown in Fig. 4. The average grain size ($\varnothing_{li}$) was determined by the lineal intercept method [40]. The ceramic bodies sintered at 1150 °C and 1200 °C show globular-like and irregular grains between 0.25 and 0.65 µm ($\varnothing_{li}$ = 0.4 µm) and 0.4–2.6 µm ($\varnothing_{li}$ = 1.3 µm), respectively. After heating to 1250 °C the grain size range is between 0.7 and 4.1 µm ($\varnothing_{li}$ = 2.1 µm) and grows to 0.8–5.5 µm ($\varnothing_{li}$ = 2.4 µm) at 1325 °C (Fig. 4a,b). Sintering at 1350 °C leads to a drastic change of the microstructure consisting of small rods with dimensions up to 4 µm in length and up to 1 µm in width. (Fig. 4c). After sintering at 1400 °C areas with small rods and very large crystals up to 200 µm in length occur (Fig. 4d). The surrounding of these large crystals, has the same microstructure as the

ceramic sintered at 1350 °C. The ceramic body shows about 1 µm wide cracks probably caused by the formation of the large crystals inside a matrix of small rods.

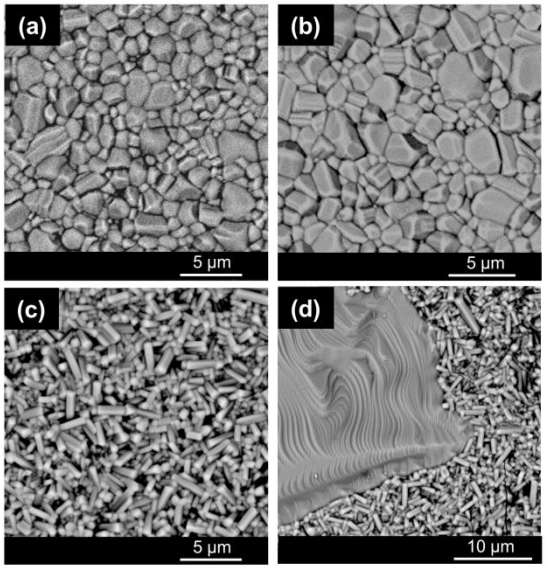

Fig. 4: SEM-BSE images of the microstructure of selected ceramic bodies sintered at (a) 1250 °C/ 10 h, (b) 1325 °C/ 10 h, c) 1350 °C/ 10 h, and d) 1400 °C/ 10 h.

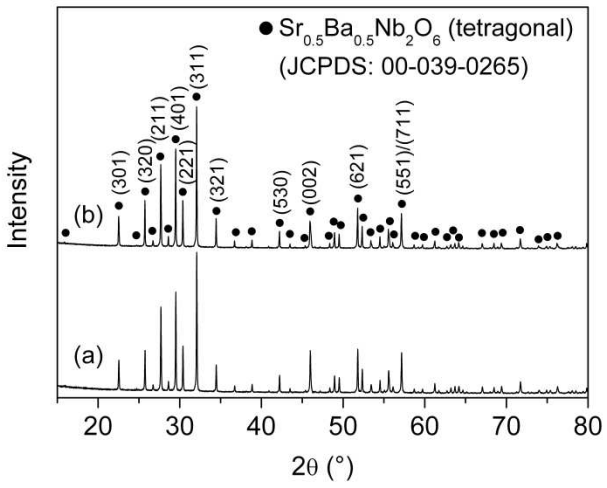

Fig. 5: Room temperature XRD patterns of $Sr_{0.5}Ba_{0.5}Nb_2O_6$ ceramics sintered at a) 1150 °C/ 10 h and b) 1400 °C/ 10 h.

Additional values for further sintering temperatures are listed in Tab. S1 (supporting information). XRD patterns of powdered ceramic bodies sintered between 1150 and 1400 °C show only reflections of $Sr_{0.5}Ba_{0.5}Nb_2O_6$ (Fig. 5). The XRD patterns of the ceramics were refined on the basis of a primitive tetragonal unit cell (space group P4bm, no. 100) according to Rathore and Vitta [25]. The cell metric of the ceramic sintered at 1150 °C was calculated as a = b = 1247.74(3) and c = 394.56(2) pm (see also Fig. S1, supporting information) which agrees very well with previously reported data [25,41,42]. With increasing sintering temperature the cell parameters do not change significantly.

3.3 Thermoanalytic, UV-Vis, and dielectric measurements

In literature, the reported melting point of $Sr_{0.5}Ba_{0.5}Nb_2O_6$ differs between 1480 °C and about 1500 °C [10,43,44–47]. For our examination of the melting point ceramic bodies sintered at 1300 °C for 10 h were crushed into fine powders. DSC measurements were done in a platinum crucible in flowing nitrogen atmosphere (Fig. S2, supporting information). The melting temperature (onset of the melting peak) was determined to 1506(7) °C and from the peak area the enthalpy of fusion is ΔH_f = 140(20) kJ mol^{-1} which corresponds to ΔS_f = 79(12) J mol^{-1} K^{-1}. The DSC investigations with $Sr_{0.5}Ba_{0.5}Nb_2O_6$ prepared by the conventional mixed-oxide method resulting in very similar values of 1504(7) °C and ΔH_f = 130(20) kJ mol^{-1}. To our best knowledge, the enthalpy of fusion for $Sr_{0.5}Ba_{0.5}Nb_2O_6$ was never reported before. For comparison, the enthalpy of fusion of Nb_2O_5 is 103 kJ mol^{-1} [48]. The XRD patterns of the transparent melts show single-phase $Sr_{0.5}Ba_{0.5}Nb_2O_6$ indicating congruent melting.

The thermal expansion of polycrystalline bulk ceramics was determined by dilatometric measurements (inset in Fig. S2, supporting information) [49,50,68]. Investigations up to 500 °C reveal an average linear thermal expansion coefficient of $\alpha_{dil} = 10.5(5)\cdot10^{-6}$ K^{-1}.

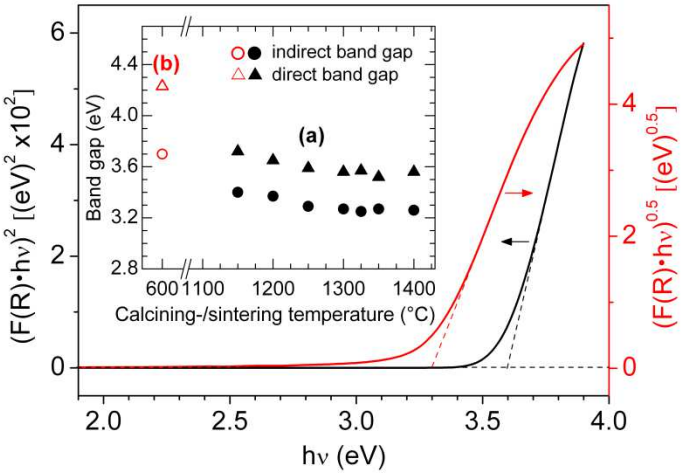

Fig. 6: $(F(R)\cdot h\nu)^n$ versus hν (n = 2 and 0.5) of the ceramic sintered at 1250 °C/ 10 h. The inset shows the calculated indirect-allowed and direct-allowed band gap energies of ceramics sintered between 1150 and 1400 °C/ 10 h (a) as well as of the preceramic nano-crystalline powder calcined at 600 °C/ 2 h (b). The uncertainties (≤ 0.05 eV) of the band gap values are smaller than the symbol size.

Diffuse reflectance spectra were recorded of the nano-crystalline powder calcined at 600 °C for 2 h and of powdered $Sr_{0.5}Ba_{0.5}Nb_2O_6$ ceramics (see also Fig. S3, supporting information). The *Kubelka–Munk* theory was used for determining the optical band gap [51,52] and the reflectance data were combined with the absorption coefficient according to Eq. 1:

$$F(R) = \frac{\alpha}{s} = \frac{(1-R)^2}{2R} \qquad (1)$$

($F(R)$ – Kubelka–Munk function, R – reflectance, α – absorption coefficient, s – scattering factor). Since $F(R)$ is proportional α (s is wavelength-independent [52]) the optical band gap can be expressed by Eq. 2 [53,54]:

$$F(R)\cdot h\nu = k(h\nu - E_g)^{1/n} \qquad (2)$$

(k – energy-independent constant, E_g – optical band gap, n – exponent reflecting the type of transition). For direct-allowed transitions n = 2, for indirect-allowed transitions n = 1/2 and

for direct- and indirect-forbidden transitions n = 2/3 and 1/3, respectively. The optical band gap can be determined by plotting of $(F(R) \cdot h\nu)^n$ vs. $h\nu$ and extrapolating the slope to $F(R) \rightarrow 0$. In literature, direct-allowed as well as indirect-allowed transition mechanisms were assumed to calculate the band gap energy for $Sr_{0.5}Ba_{0.5}Nb_2O_6$ [55–59]. As demonstrated in Fig. 6 the indirect and direct optical band gap can be obtained by plotting of $(F(R) \cdot h\nu)^{0.5}$ and $(F(R) \cdot h\nu)^2$ vs. $h\nu$, respectively. Often, the *McLean* analysis [53,60] of the absorption edge is used to find the type of transition (n). Unfortunately, for our spectra this analysis did not lead to a clear result. As an alternative approach, the exponent n can also be estimated by linearization of Eq. 2 [61–63]:

$$\ln(F(R)\cdot h\nu) = \ln k + n^{-1} \ln(h\nu - E_g) \qquad (3)$$

Building the derivative of this expression leads to:

$$\frac{\mathrm{d}(\ln(F(R)\cdot h\nu)}{\mathrm{d}(h\nu)} = \frac{1}{n\cdot(h\nu - E_g)} \qquad (4)$$

A plot of $\mathrm{d}(\ln(F(R)\cdot h\nu)/\mathrm{d}(h\nu)$ vs. $h\nu$ thus shows a maximum around E_g. This approximated E_g value was used to determine n, which can be obtained as the inverse slop in the plot of $\ln(F(R)\cdot h\nu)$ vs. $\ln(h\nu - E_g)$ (Fig. 7). The value of n was found to be ~0.5 for all samples indicating an indirect-allowed transition in accordance with band structure calculations by *Andriyevsky* et al. [64] for $Sr_{0.60}Ba_{0.40}Nb_2O_6$.

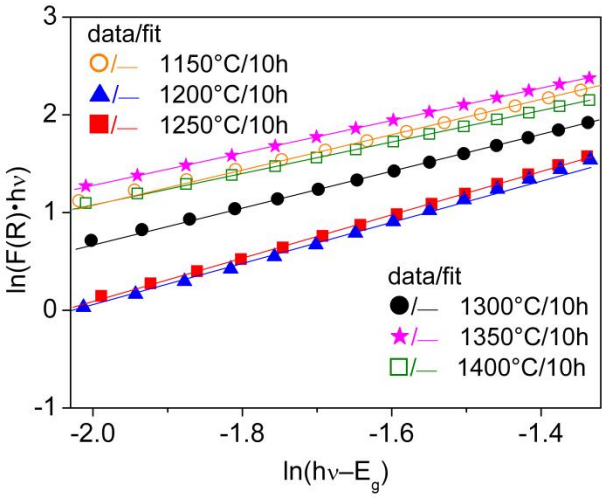

Fig. 7: ln(F(R)·hν) versus ln(E–E_g) for powdered ceramics after various sintering temperatures.

The indirect-allowed optical band gap for the nano-sized preceramic powder, calcined at 600 °C, was calculated as 3.70(5) eV. After ten-hour sintering of that nano-powder at 1150 °C the band gap is 3.40(4) eV which decreases to 3.29(5) eV after sintering at 1250 °C and does not change significantly up to 1400 °C (inset in Fig. 6). The considerably higher band gap energy for the nano-sized sample is most likely due to the well-known size effect leading to a blue shift of the absorption edge with decreasing particle size [65–69]. For comparative purposes with literature data, the band gap values assuming a direct allowed transition accounts to 4.23(5) eV and is reduced to 3.59(5) eV after heating to 1250 °C (inset in Fig. 6).

Fig. 8 shows frequency-dependent room-temperature (23 °C) dielectric measurements of ceramic bodies between 0.5 kHz and 1 MHz, based on impedance measurements using the model of a lossy capacitor. The samples show only slightly decreasing relative permittivities (ε_r) with increasing frequency. The relative permittivities become larger with sintering temperature up to 1325 °C due to an increase in densities and grain sizes (see also Tab. S1, supporting information). The sample sintered at 1350 °C reveals lower permittivity values most probably caused by a change in the rode-type microstructure as described above.

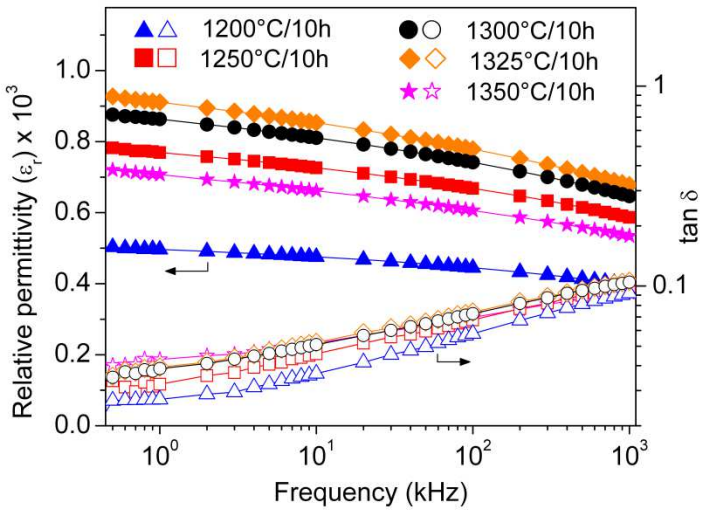

Fig. 8: Frequency dependence of the real part of the relative permittivity (closed symbols) and the dissipation factor (open symbols) at 23 °C for ceramic bodies sintered at the indicated temperatures. The uncertainty of the data is smaller than the symbol size and is lower than 5 %.

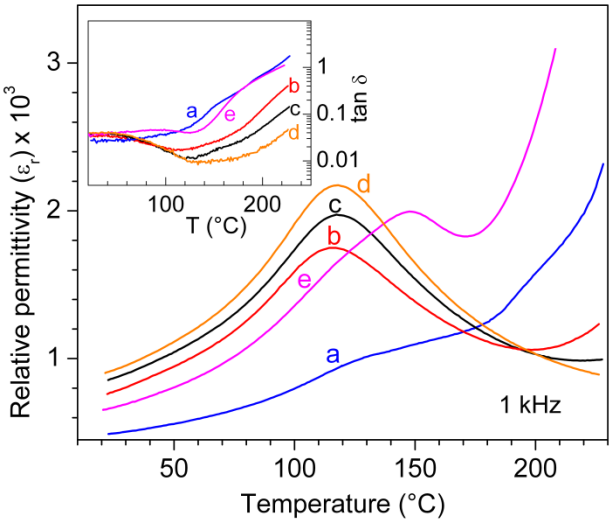

Fig. 9: Temperature dependence of ε_r and tan δ (inset) at 1 kHz for ceramic bodies sintered at different temperatures for 10 h. a) 1200 °C, b) 1250 °C, c) 1300 °C, d) 1325 °C, e) 1350 °C.

The temperature dependence of the relative permittivity and the dissipation factor at 1 kHz is shown in Fig. 9. The dense ceramic bodies sintered at 1250, 1300, and 1325 °C show a broad maximum of ε_r at 116(1) °C, 118(1) °C, and 118(1) °C indicating a diffuse ferroelectric–paraelectric phase transition. The maximum value of ε_r increases slightly with

sintering temperature from 1750 to 2170 due to the increase in density and grain size. The ceramic sintered at 1200 °C does not show a clear phase transition at 1 kHz, because of its low density and smaller grain sizes. The sample sintered at 1350 °C shows a deviating behavior with a maximum of ε_r of 1990 at 147(1) °C caused by the rod-like microstructure. The dielectric response at frequencies above 1 kHz for samples sintered at 1200 and 1350 °C show decreasing permittivity values above the maximum (Fig. S4, supporting information).

The temperature of the permittivity maximum (T_m) is slightly shifted to higher temperatures with rising frequencies (Fig. S5, supporting information). The shift of T_m from 1 kHz to 1 MHz was found to be in the range of 4–5 K. The dielectric response above T_m deviated from the normal Curie-Weiss law indicating a relaxor-like behavior [70]. As proposed in literature [71–73], the dielectric behavior of a relaxor ferroelectric can be described by a modified Curie-Weiss law:

$$\frac{1}{\varepsilon} - \frac{1}{\varepsilon_m} = \frac{(T - T_m)^\gamma}{C'} \qquad (5)$$

where, ε_m is the permittivity maximum, T_m is the temperature at ε_m, C' is a constant, and the exponent γ is the diffuseness coefficient which describes the character of the phase transition. For a normal ferroelectric behavior is $\gamma = 1$ and for ideal relaxor ferroelectrics is $\gamma = 2$. From a plot of $\ln(\varepsilon^{-1} - \varepsilon_m^{-1})$ vs. $\ln(T - T_m)$ (Fig. S6, supporting information) we obtained values for γ between 1.70 and 1.80. The diffuseness coefficient (γ) is somewhat larger than reported values for $Sr_{0.5}Ba_{0.5}Nb_2O_6$ ceramics obtained by the conventional method [22,25,74]. This slight increase of the diffuseness of the phase transition is caused by a size-effect [75–77] due to the considerably smaller grain-sizes of the ceramics prepared by the soft-chemistry method described herein [22,23,25,26]. Moreover, the T_m values are significantly higher than reported temperatures of the permittivity maximum for ceramics prepared by other soft-chemistry

methods [17,19–21]. On the other hand, our T_m values are in accordance with temperature values of the dielectric maximum of $Sr_{0.5}Ba_{0.5}Nb_2O_6$ single-crystals [2,10,13,45,78].

The discussion above did not consider a possible dc-conductivity. In general, the conductivity of the investigated samples at low temperatures are rather low ($\sigma_{dc} << 10^{-7}$ S cm^{-1}) so that the model of a lossy capacitor described above can be well used. In contrast, the samples exhibit pronounced dc-conductivities at elevated temperatures indicating a semiconducting nature. The high-temperature impedance data were modelled using equivalent circuits consisting of one or two parallel resistance-capacitor (RC) elements. The specific complex impedance (ρ^*) for a single RC element is described by:

$$\rho^* = \frac{\rho_{dc}}{1+(i\omega\tau)^{\beta}} \qquad (6)$$

where, β is the constant phase shift (CPE) coefficient and $\tau = \rho_{dc}\varepsilon\varepsilon_0$. Details of this approach have been reported elsewhere [79]. The Cole-Cole plot of the specific complex impedance for the ceramic sintered at 1200 °C reveals two semicircle arcs and can be well described by two RC elements connected in series indicating two different electrical transport processes (Fig. S7a, supporting information). The derived relative permittivities of 2550 and 86600 can be assigned to contributions of the bulk and grain boundaries, respectively, based on the reasoning by *Irvine* et al. [80] that the grain boundary capacitance and thus the permittivity values are at least one order of magnitude higher than bulk permittivities. Cole–Cole plots of the other ceramics sintered from 1250 to 1325 °C reveal one single semicircular arc (Fig. S7b, supporting information) indicating a single relaxation process. Because of the high density and larger grain sizes of these ceramics compared to the one sintered at 1200 °C this single relaxation process is assigned to the bulk effect only. This assignment is supported by the fact that the calculated permittivity values vary between 1600 and 2400 and are therefore

comparable to the bulk contribution found for the aforementioned ceramic sintered at 1200 °C. After sintering at 1350 °C the Cole-Cole plot can be still fitted by one RC element (Fig. S7c, supporting information); however, a closer inspection indicates the beginning of a second semicircular arc in the low frequency region (marked by a dotted circle in the figure). This second circle suggests a possible grain boundary contribution besides the bulk effect, which arises from the change of the microstructure which consists of rods with a maximum thickness of 1 µm, whose occurrence may be the main reason for the observed additional grain boundary contribution.

4. Conclusion

A nano-crystalline $Sr_{0.5}Ba_{0.5}Nb_2O_6$ powder with a crystallite size of 24(2) nm and a specific surface area of 38.5(10) $m^2\ g^{-1}$ was synthesized by a polymerization route using PEG400 and following calcination at 600 °C. From this nano-crystalline powder ceramic bodies with variable grain sizes and a fine-grained microstructure are available. Dense ceramics (relative density ≥ 90 %) can be obtained after sintering above 1200 °C. The indirect-allowed optical band gap of the nano-powder is 3.70(5) eV and decreases to 3.29(5) eV upon sintering. The melting temperature and enthalpy of fusion were determined as 1506(7) °C and ΔH_f = 140(20) kJ mol^{-1}. The average linear thermal expansion coefficient was found to be $10.5(5)\cdot10^{-6}\ K^{-1}$. Dielectric measurements were carried out revealing a diffuse ferroelectric–paraelectric phase transition which occurs around 120 °C and permittivity maxima up to 2170. The temperature of the permittivity maximum shifts slightly with raising frequency indicating a relaxor behavior. At elevated temperatures around 220–240 °C, the impedance data can be fitted using an equivalent circuit consisting of one or two RC elements that allows to distinguish between grain boundary and bulk contributions. The synthesis route described in this article leads to the formation of $Sr_{0.5}Ba_{0.5}Nb_2O_6$ at much lower calcining temperature compared to

other soft-chemistry syntheses. The microstructure of resulting ceramics show significant smaller grain sizes compared to conventional syntheses. Furthermore, the temperature of the diffuse phase transition agrees well with values for single-crystals in contrast to other reported soft-chemistry syntheses.

Acknowledgments

This publication was funded by the German Research Foundation within the Collaborative Research Centre 762 (project A8).

Appendix A. Supplementary data

Supplementary data associated with this article can be found, in the online version, at http://dx.doi.org/

References

[1] V. D. Antsigin, E. G. Kostov, V. K. Malinovsky, L. N. Sterelyukhina, Electrooptics of Thin Ferroelectric Films, Ferroelectrics 38 (1981) 761–763.

[2] A. M. Glass, Investigation of the Electrical Properties of $Sr_{1-x}Ba_xNb_2O_6$ with Special Reference to Pyroelectric Detection, J. Appl. Phys. 40 (1969) 4699–4713.

[3] D. Rytz, B. A. Wechsler, R. N. Schwartz, C. C. Nelson, C. D. Brandle, A. J. Valentino, G. W. Berkstresser, Temperature Dependence of Photorefractive Properties of Strontium-Barium Niobate ($Sr_{0.6}Ba_{0.4}Nb_2O_6$), J. Appl. Phys. 66 (1989) 1920–1924.

[4] S. T. Liu and L. E. Cross, Primary Pyroelectricity in Strontium Barium Niobate ($Sr_{0.5}Ba_{0.5}Nb_2O_6$) Single Crystals, phys. stat. sol. 41 (1977) K83–K87.

[5] R. R. Neurgaonkar and L. E. Cross, Piezoelectric Tungsten Bronze Crystals for SAW Device Applications, Mater. Res. Bull. 21 (1989) 893–899.

[6] T. Lukasiewicz, M. A. Swirkowicz, J. Dec, W. Hofman, W. Szyrski, Strontium–Barium Niobate Single Crystals, Growth and Ferroelectric Properties, J. Cryst. Growth 310 (2008) 1464–1469.

[7] G. Han, S. Cao, B. Lin, UV Photocatalytic Activity for Water Decomposition of $Sr_xBa_{1-x}Nb_2O_6$ Nanocrystals with Different Components and Morphologies, J. Chem. (2017) 2163608.

[8] K. Yoshida, H. Masai, Y. Takahashi, R. Ihara, T. Fujiwara, Fabrication of $Sr_{0.5}Ba_{0.5}Nb_2O_6$-precipitated Microstructured Ceramics for Photocatalytic Application, J. Ceram. Soc. Jpn. 119 (2011) 731–735.

[9] D. Fan, R. Chong, F. Fan, X. Wang, C. Li, Z. Feng, A Tetragonal Tungsten Bronze-type Photocatalyst: Ferro-Paraelectric Phase Transition and Photocatalysis, Chin. J. Catal. 37 (2016) 1257–1262.

[10] A. A. Ballmann and H. Brown, The Growth and Properties of Strontium Barium Metaniobate $Sr_xBa_{1-x}Nb_2O_6$, A Tungsten Bronze Ferroelectric, J. Cryst. Growth 1 (1967) 311–314.

[11] P. B. Jamieson, S. C. Abrahams, J. L. Bernstein, Ferroelectric Tungsten Bronze-Type Crystal Structures. I. Barium Strontium Niobate $Ba_{0.27}Sr_{0.75}Nb_2O_{5.78}$, J. Chem. Phys. 48 (1968) 5048–5057.

[12] W. H. Huang, Dwight Viehland, R. R. Neurgaonkar, Anisotropic Glasslike Characteristics of Strontium Barium Niobate Relaxors, J. Appl. Phys. 76 (1994) 490–496.

[13] C. David, T. Granzow, A. Tunyagi, M. Wöhlecke, Th. Woike, K. Betzler, M. Ulex, M. Imlau, R. Pankrath, Composition Dependence of the Phase Transition Temperature in $Sr_xBa_{1-x}Nb_2O_6$, phys. stat. sol. (a) 201 (2004) R49–R52.

[14] S. H. Kshirsagar, A. N. Tarale, S. R. Jigajeni, D. J. Salunkhe, P. B. Joshi, Effect if Ni Doping on Ferroelectric, Dielectric and Magneto Dielectric Properties of Strontium Barium Niobate Ceramics, Indian J. Pure Appl. Phys. 53 (2015) 119−124.

[15] M. Said, T. S. Velayutham, W. C. Gan, W. H. Abd Majid, The Structural and Electrical Properties of $Sr_xBa_{(1-x)}Nb_2O_6$ (SBN) Ceramic with Varied Composition, Ceram. Int. 41 (2015) 7119–7124.

[16] P. K. Patro, A. R. Kulkarni, S. M. Gupta, C. S. Harendranath, Improved Microstructure, Dielectric and Ferroelectric Properties of Microwave-Sintered $Sr_{0.5}Ba_{0.5}Nb_2O_6$, Physika B 400 (2007) 237–242.

[17] P. K. Patro, R. D. Deshmukh, A. R. Kulkarni, C. S. Harendranath, Synthesis of $Sr_{0.5}Ba_{0.5}Nb_2O_6$ by Coprecipitation Method – Dielectric and Microstructural Characteristics, J. Electroceram. 13 (2004) 479–485.

[18] P. K. Patro, A. R. Kulkarni, C. S. Harendranath, Microstructure and Dielectric Properties of Strontium Barium Niobate Ceramics Synthesized by Partial Coprecipitation, J. Eur. Ceram. Soc. 23 (2003) 1329–1335.

[19] T. Chen, S. Y. Wu, X. Q. Liu, X. M. Chen, A Novel Sol–Gel Route to Synthesize $(Sr_{0.5}Ba_{0.5})Nb_2O_6$ Ceramics with Enhanced Electrocaloric Effect, J. Adv. Dielectr. 7 (2017) 1750012.

[20] S. Wanmei, L. Shijun, S. Ranran, W. Chunlong, Investigation of the Origin of Abnormal Grain Growth in the Sintering Process of $Sr_{0.5}Ba_{0.5}Nb_2O_6$ Ceramics without Eutectic Liquid-Phase, J. Ceram. Proc. Res. 12 (2011) 716–720.

[21] P. K. Patro, A. R. Kulkarni, C. S. Harendranath, Combustion Synthesis of $Sr_{0.5}Ba_{0.5}Nb_2O_6$ and Effect of Fuel on its Microstructure and Dielectric Properties, Mater. Res. Bull. 38 (2003) 249–259.

[22] M.-S. Kim, P. Wang, J.-H. Lee, J.-J. Kim, H. Y. Lee, S.-H. Cho, Site Occupancy and Dielectric Characteristics of Strontium Barium Niobate Ceramics: Sr/Ba Ratio Dependence, Jpn. J. Appl. Phys. 41 (2002) 7042−7047.

[23] S.-I. Kang, J.-H. Lee, J.-J. Kim, H. Y. Lee, S.-H. Cho, Effect of Sintering Atmosphere on Densification and Dielectric Characteristics in $Sr_{0.5}Ba_{0.5}Nb_2O_6$ Ceramics, J. Eur. Ceram. Soc. 24 (2004) 1031−1035.

[24] T.-T. Fang, N.-T. Wu, F.-S. Shiau, Formation Mechanism of Strontium Barium Niobate Ceramic Powders, J. Mater. Sci. Lett. 13 (1994) 1746–1748.

[25] S. S. Rathore and S. Vitta, Enhanced Dielectric Constant and Relaxor Behavior Realized by Dual Stage Sintering of $Sr_{0.5}Ba_{0.5}Nb_2O_6$, AIP Conf. Proc. 1591 (2014) 133−135.

[26] Y.-Q. Qu, A.-S. Li, Q.-Y. Shao, Y.-F. Tang, D. Wu, C. L. Mak, K. H. Wong, N.-B. Ming, Structure and Electric Properties of Strontium Barium Niobate Ceramics, Mater. Res. Bull. 37 (2002) 503−513.

[27] C. M. Dudhe, S. B. Nagdeot, C. P. Chaudhari, Ferroelectric Domains in $Sr_{0.5}Ba_{0.5}Nb_2O_6$ (SBN50) at Nanolevel, Ferroelectrics 482 (2015) 104–112.

[28] R. Pasricha and V. Ravi, Synthesis of $Sr_{0.5}Ba_{0.5}Nb_2O_6$ by Citrate Gel Method, Mater. Chem. Phys. 94 (2005) 34–36.

[29] S.-G. Lu, C.-L. Mak, K.-H. Wong, Low-Temperature Preparation and Size Effect of Strontium Barium Niobate Ultrafine Powder, J. Am. Ceram. Soc. 84 (2001) 79–84.

[30] Y. Li, J. Zhao, B. Wang, Low Temperature Preparation of Nanocrystalline $Sr_{0.5}Ba_{0.5}Nb_2O_6$ Powders Using an Aqueous Organic Gel Route, Mater. Res. Bull. 39 (2004) 365–374.

[31] S. R. Dhage, R. Pasricha, V. Ravi, Synthesis of $Sr_{0.5}Ba_{0.5}Nb_2O_6$ by Urea Method, Mater. Lett. 59 (2005) 1053–1055.

[32] A. B. Panda, A. Pathak, P. Pramanik, Low Temperature Preparation of Nanocrystalline Solid Solution of Strontium–Barium–Niobate by Chemical Process, Mater. Lett. 52 (2002) 180−186.

[33] Program WinXPOW v2.11, Stoe & Cie GmbH, Darmstadt, 2004.

[34] W. Kraus, G. Nolze, PowderCell 2.0 for Windows, Powder Diffr. 13 (1998) 256–259

[35] J. Rodriguez-Carvajal, Recent advances in magnetic structure determination by neutron powder diffraction, Physica B 192(1993) 55–69.

[36] I. C. Madsen, N. V. Y. Scarlett, A. Kern, Description and Survey of Methodologies for the Determination of Amorphous Content via X-ray Powder Diffraction, Z. Kristallogr. 226 (2011) 944–955.

[37] R. S. Winburn, D. G. Grier, G. J. McCarthy, R. B. Peterson, Rietveld Quantitative X-ray Diffraction Analysis of NIST Fly Ash Standard Reference Materials, Powder Diffr. 15 (2000) 163−172.

[38] A. G. De La Torre, S. Bruque, M. A. G. Aranda, Rietveld Quantitative Amorphous Content Analysis, J. Appl. Cryst. 34 (2001) 196–202.

[39] C. S. Dandeneau, T. W. Bodick, R. K. Bordia, F. S. Ohuchi, Thermoelectric Properties of Reduced Polycrystalline $Sr_{0.5}Ba_{0.5}Nb_2O_6$ Fabricated Via Solution Combustion Synthesis, J. Am. Ceram. Soc. 96 (2013) 2230–2237.

[40] M. I. Mendelson, Average Grain Size in Polycrystalline Ceramics, J. Am. Ceram. Soc. 52 (1969) 443–446.

[41] S. Podlozhenov, H. A. Graetsch, J. Schneider, M. Ulex, M. Wöhlecke, K. Betzler, Structure of Strontium Barium Niobate $Sr_xBa_{1-x}Nb_2O_6$ (SBN) in the Composition Range $0.32 \leq x \leq 0.82$, Acta Cryst. B62 (2006) 960–965.

[42] T. S. Chernaya, T. R. Volk, I. A. Verin, L. I. Ivleva, V. I. Simonov, Atomic Structure of $(Sr_{0.50}Ba_{0.50})Nb_2O_6$ Single Crystals in the Series of $(Sr_xBa_{1-x})Nb_2O_6$ Compounds, Crystallogr. Rep. 47 (2002) 213–216.

[43] P. Reiche, R. Schalge, J. Bohm, D. Schultze, Growth of Defect-free $Sr_{1-x}Ba_xNb_2O_6$ (SBN) Crystals, Kristall u. Technik 15 (1980) 23–28.

[44] C. Nikasch and M. Göbbels, Phase Relations and Lattice Parameters in the System SrO–BaO–Nb_2O_5 Focusing on SBN ($Sr_xBa_{1-x}Nb_2O_6$), J. Cryst. Growth 269 (2004) 324–332.

[45] R. B. Maciolek and S. T. Liu, Preparation and Properties of Low Loss $Sr_{1-x}Ba_xNb_2O_6$ Ferroelectric Single Crystals, J. Electron. Mater. 2 (1973) 191–200.

[46] J. R. Carruthers and M. Grasso, Phase Equilibria Relations in the Ternary System BaO-SrO-Nb_2O_5, J. Electrochem. Soc. 117 (1970) 1426–1430.

[47] M. Ulex, R. Pankrath, K. Betzler, Growth of Strontium Barium Niobate: the Liquidus–Solidus Phase Diagram, J. Cryst. Growth 271 (2004) 128–133.

[48] K. K. Kelly High-Ttemperature Heat-Content, Heat-Capacity, and Entropy Data for the Elements and Inorganic Compounds, Bureau of Mines Bulletin 584 (1960), p. 131.

[49] W. F. Hemminger, H. K. Cammenga, Methoden der Thermischen Analyse, Springer-Verlag, Berlin-Heidelberg, 1989.

[50] J. D. James, J. A. Spittle, S. G. R. Brown, R. W. Evans, A Review of Measurement Techniques for the Thermal Expansion Coefficient of Metals and Alloys at Elevated Temperatures, Meas. Sci. Technol. 12 (2001) R1–R15.

[51] P. Kubelka and F. Munk, Ein Beitrag zur Optik der Farbanstriche, Z. Techn. Phys. 11 (1931) 593–601.

[52] G. Kortüm and J. Vogel, Die Theorie der diffusen Reflexion von Licht an pulverförmigen Stoffen, Z. Phys. Chem. 18 (1958) 110–122.

[53] M. Nowak, B. Kauch, P. Szperlich, Determination of Energy Band Gap of Nanocrystalline SbSI Using Diffuse Reflectance Spectroscopy, Rev. Sci. Instrum. 80 (2009) 046107.

[54] O. Schevciw and W. B. White, The Optical Absorption Edge of Rare Earth Sesquisulfides and Alkaline Earth – Rare Earth Sulfides, Mater. Res. Bull. 18 (1983) 1059–1068.

[55] M.-H. Li, T.-C. Chong, X.-W Xu, H. Kumagai, Growth and Spectra Characterization of Ce and Eu Doped SBN Crystals, J. Cryst. Growth 225 (2001) 479–483.

[56] J. Nuja, C. S. Suchand Sandeep, Philip Reji, and K. Nandakumar, Nonlinear Optical Properties of Nanosized Rare-Earth–Doped Strontium Barium Niobate Ceramics, Spectrosc. Lett. 44 (2011) 334–339.

[57] S. G. Lu, C. L. Mak, K. H. Wong, Optical Studies of Transparent Ferroelectric Strontium–Barium Niobate/Silica Nanocomposite, J. Appl. Phys. 94 (2003) 3422–3426.

[58] D. Fan, J. Zhu, X. Wang, S. Wang, Y. Liu, R. Chen, Z. Feng, F. Fan, C. Li, Dual Extraction of Photogenerated Electrons and Holes from a Ferroelectric $Sr_{0.5}Ba_{0.5}Nb_2O_6$ Semiconductor, ACS Appl. Mater. Interfaces 8 (2016) 13857−13864.

[59] F. P. Koffyberg, K. Dwight, A. Wold, Interband Transition of Semiconducting Oxides Determined from Photoelectrolysis Spectra, Solid State Comm. 30 (1979) 433–437.

[60] T.P McLean, in: A.F. Gibson (Ed.), Progress in Semiconductors, Vol. 5, 1960, pp. 55−102.

[61] D. Bjattacharyya, S. Chaudhuri, A. K. Pal, Bandgap and Optical Transitions in Thin Films from Reflectance Measurements, Vacuum 43 (1992) 313–316.

[62] F. Yakuphanoglu and M. Arslan, Determination of Electrical Conduction Mechanism and Optical Band Gap of a New Charge Transfer Complex: TCNQ-PANT, Solid State Comm. 132 (2004) 229–234.

[63] J. Tang, Z. Zou, J. Ye, Photophysical and Photocatalytic Properties of $AgInW_2O_8$, J. Phys. Chem. B 107 (2003) 14265–14269.

[64] B. Andriyevsky, A. Patryn, K. Dorywalski, C. Cobet , M. Piasecki, I. Kityk, N. Esser, T. Łukasiewicz, J. Dec, Electronic and Optical Properties of Strontium Barium Niobate Single Crystals, Ferroelectrics 426 (2012) 194–205.

[65] S. N. Sahu and K. K. Nanda, Nanostructure Semiconductors: Physics and Applications, PINSA A67 (2001) 103–130.

[66] L. E. Brus, Electron–electron and electron-hole interactions in small semiconductor crystallites: The size dependence of the lowest excited electronic state, J. Chem. Phys. 80 (1984) 4403.

[67] M.-M. Bagheri-Mohagheghi, N. Shahtahmasebi, N. R. Alinejad, A. Youssefi, M. Shokooh-Saremi, The effect of the post-annealing temperature on the nano-structure and energy band gap of SnO2 semiconducting oxide nano-particles synthesized by polymerizing–complexing sol–gel method, Physica B 403 (2008) 2431–2437.

[68] R. Köferstein and S. G. Ebbinghaus, Investigations of $BaFe_{0.5}Nb_{0.5}O_3$ Nano Powders Prepared by a Low Temperature Aqueous Synthesis and Resulting Ceramics, J. Eur. Ceram. Soc. 37 (2017) 1509–1516.

[69] G. Zhang, J. Yang, S. Zhang, Q. Xiong, B. Huang, J. Wang, W. Gong, Preparation of nanosized Bi3NbO7 and its visible-light photocatalytic property, J. Hazard Mater. 172 (2009) 986–992.

[70] L. E. Cross, Relaxor Ferroelectrics: An Overview, Ferroelectrics 151 (1994) 305–320.

[71] X. G. Tang, K.-H. Chew, H. L. W. Chan, Diffuse Phase Transition and Dielectric Tunability of $Ba(Zr_yTi_{1-y})O_3$ Relaxor Ferroelectric Ceramics, Acta Mater. 52 (2004) 5177–5183.

[72] H. T. Martirena and J. C. Burfoot, Grain-size and Pressure Effects on the Dielectric and Piezoelectric Properties of Hot-Pressed PZT-5, Ferroelectrics 7 (1974) 151–152.

[73] K. Uchino and S. Nomura, Critical Exponents of the Dielectric Constants in Diffused-Phase-Transition Crystals, Ferroelectrics 44 (1982) 55–61.

[74] S. H Kshirsagar, S. R. Ligajeni, A. N. Tarale, D. J. Salunkhe, P. B. Joshi, Investigations on Fe-doped Strontium Barium Niobate, Single Phase Ferroelectric and Magnetodielectric Compounds, J. Adv. Dielectr. 5 (2015) 1550001.

[75] J. Hao, W. Bai, W. Li, J. Zhai, Correlation Between the Microstructure and Electrical Properties in High-Performance $(Ba_{0.85}Ca_{0.15})(Zr_{0.1}Ti_{0.9})O_3$ Lead-Free Piezoelectric Ceramics, J. Am. Ceram. Soc. 95 (2012) 1998–2006.

[76] X.-G. Tang and H. L.-Wah. Chan, Effect of Grain Size on the Electrical Properties of $(Ba,Ca)(Zr,Ti)O_3$ Relaxor Ferroelectric Ceramics, J. Appl. Phys. 97 (2005) 034109.

[77] R. Köferstein, L. Jäger, M. Zenkner, S. G. Ebbinghaus, Phase Transition and Dielectric Properties of $BaTiO_3$ Ceramics Containing 10 mol% $BaGeO_3$, Mater. Chem. Phys. 119 (2010) 118–122.

[78] R. R. Neurgaonkar , W. F. Hall , J. R. Oliver , W. W. Ho, W. K. Cory, Tungsten Bronze $Sr_{1-x}Ba_xNb_2O_6$: A Case History of Versatility, Ferroelectrics 87 (1988) 167–179.

[79] F. Oehler, H.-T. Langhammer, S. G. Ebbinghaus, Preparation and Dielectric Properties of $CaTaO_2N$ and $SrNbO_2N$ Ceramics, J. Eur. Ceram. Soc. 37 (2017) 2129–2136.

[80] J. T. S. Irvine, D. C. Sinclair, A. R. West, Electroceramics: Characterization by Impedance Spectroscopy, Adv. Mater. 2 (1990) 132–138.

Supporting Information

Investigations of nano-crystalline $Sr_{0.5}Ba_{0.5}Nb_2O_6$ and bulk ceramics synthesized by a polymerization method using PEG400

Roberto Köferstein*, Florian Oehler, and Stefan G. Ebbinghaus

Institute of Chemistry, Martin Luther University Halle-Wittenberg,

Kurt-Mothes-Straße 2, 06120 Halle, Germany.

* Corresponding author. Tel.: +49-345-5525630; Fax: +49-345-5527028.

E-mail addresses: roberto.koeferstein@chemie.uni-halle.de

Table S1

Grain sizes and dielectric values of ceramic bodies

Sintering regime [1)]	Average grain size [2)] (Grain size range)	ε_r [3)]	tan δ [3)]
1150 °C, 10 h	0.4 µm (0.25–0.65 µm)	-	-
1200 °C, 10 h	1.3 µm (0.4–2.6 µm)	496	0.027
1250 °C, 10 h	2.1 µm (0.7–4.1 µm)	769	0.032
1300 °C, 10 h	2.3 µm (0.8–5.1 µm)	863	0.039
1325 °C, 10 h	2.4 µm (0.8–5.5 µm)	911	0.039
1350 °C, 10 h	rods up to 4 x 1 µm	707	0.043
1400 °C, 10 h [4)]	rods up to 4 x 1 µm, large crystals up to 200 x 70 µm	-	-

1) Temperature rate 5 K min^{-1}; 2) Lineal intercept method; 3) 23 °C, 1 kHz; 4) Sample shows some cracks

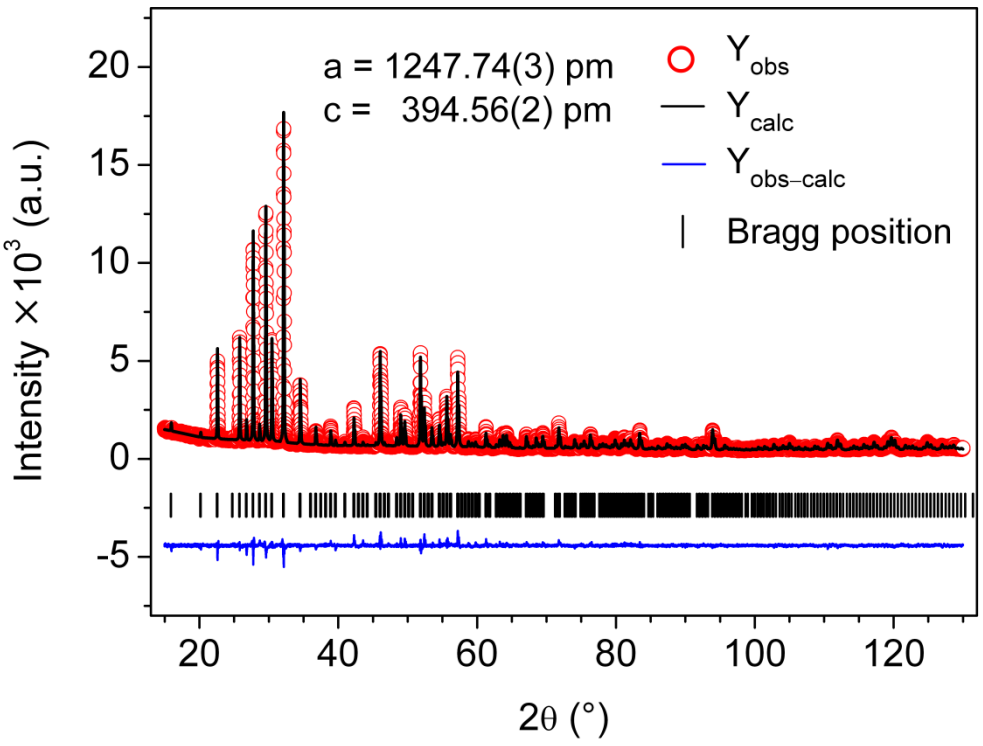

Fig. S1: Rietveld refinement (Cu-Kα1+α2 radiation) of a ceramic sample sintered at 1150 °C for 10 h. (Rp = 4.47%, Rwp = 5.85%, and χ^2 = 2.81).

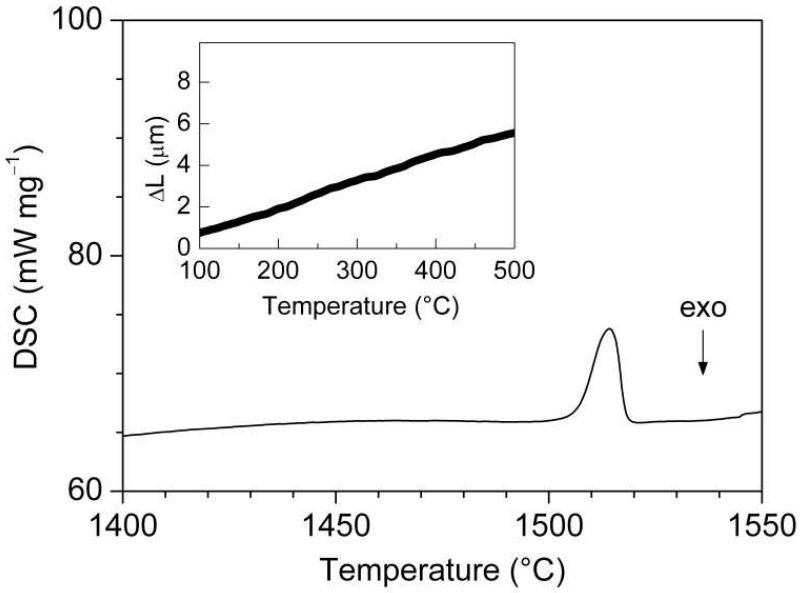

Fig. S2: DSC investigation of a powdered ceramic in flowing nitrogen atmosphere (heating rate 10 K min^{-1}). The inset shows the dilatometric measurement of a dense ceramic body (heating rate 5 K min^{-1}, flowing air).

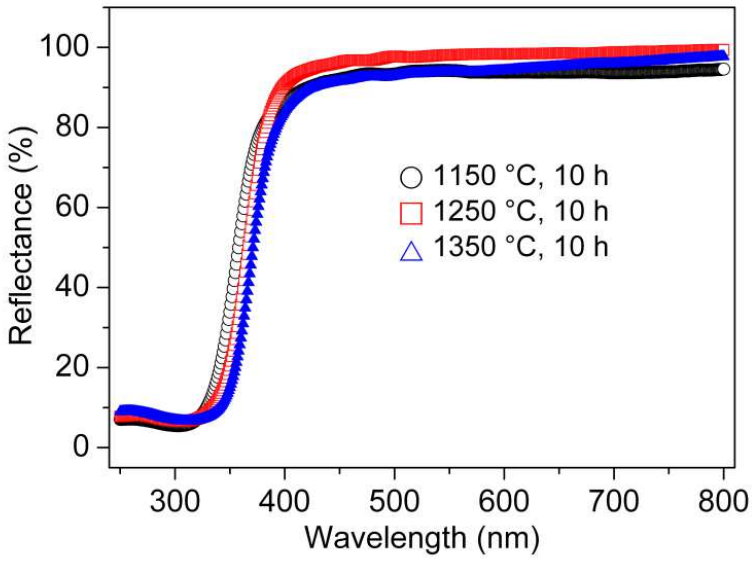

Fig. S3: Diffuse reflectance spectra of powdered ceramics after sintering at the indicated temperatures.

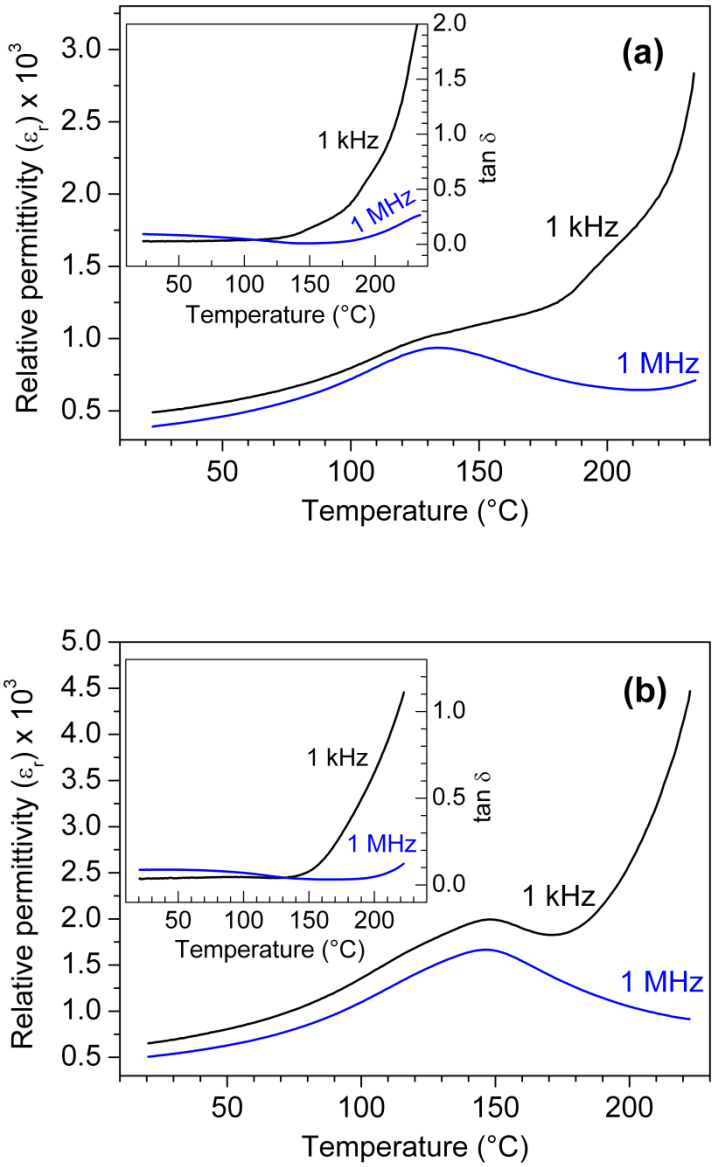

Fig. S4: Temperature dependence of the real part of the permittivity and dissipation factor (inset) at 1 kHz and 1 MHz for ceramic bodies sintered at (a) 1200 °C, 10 h and (b) 1350 °C, 10 h.

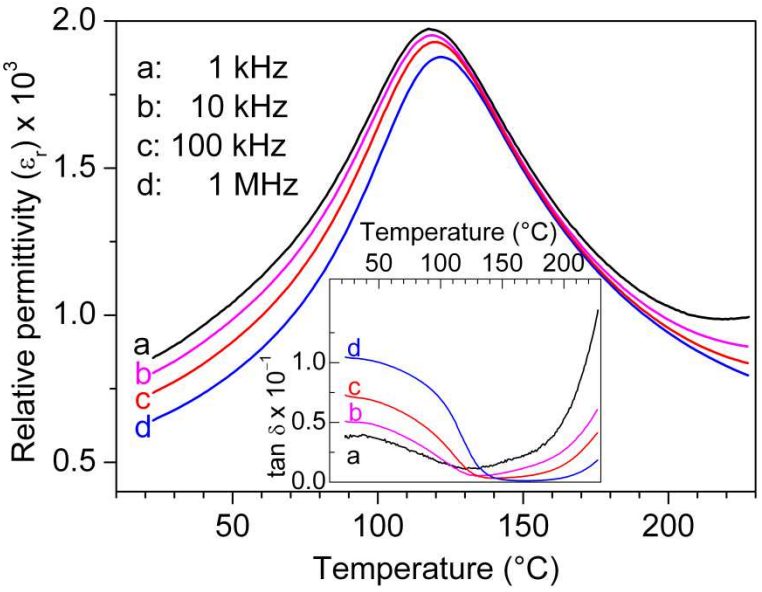

Fig. S5: Temperature dependence of ε_r and tan δ (inset) at various frequencies for a ceramic body sintered at 1300 °C for 10 h.

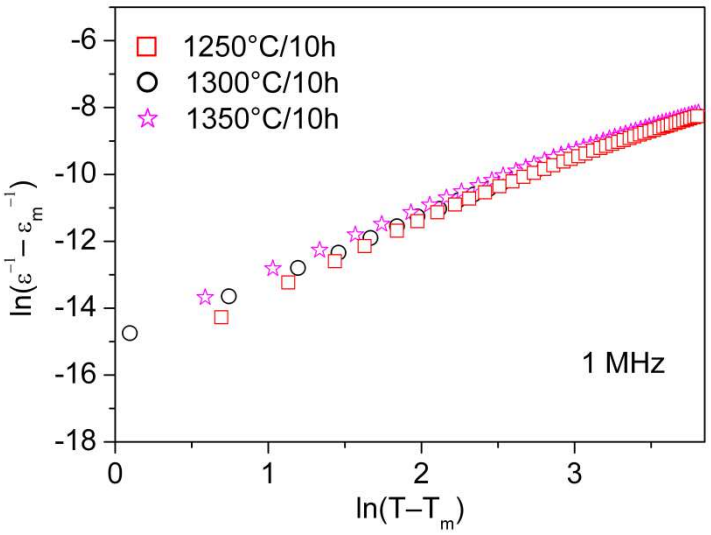

Fig. S6: Plot of $\ln(\varepsilon^{-1} - \varepsilon_m^{-1})$ as a function of $\ln(T-T_m)$ for $Sr_{0.5}Ba_{0.5}Nb_2O_6$ ceramics samples sintered at the indicated temperatures.

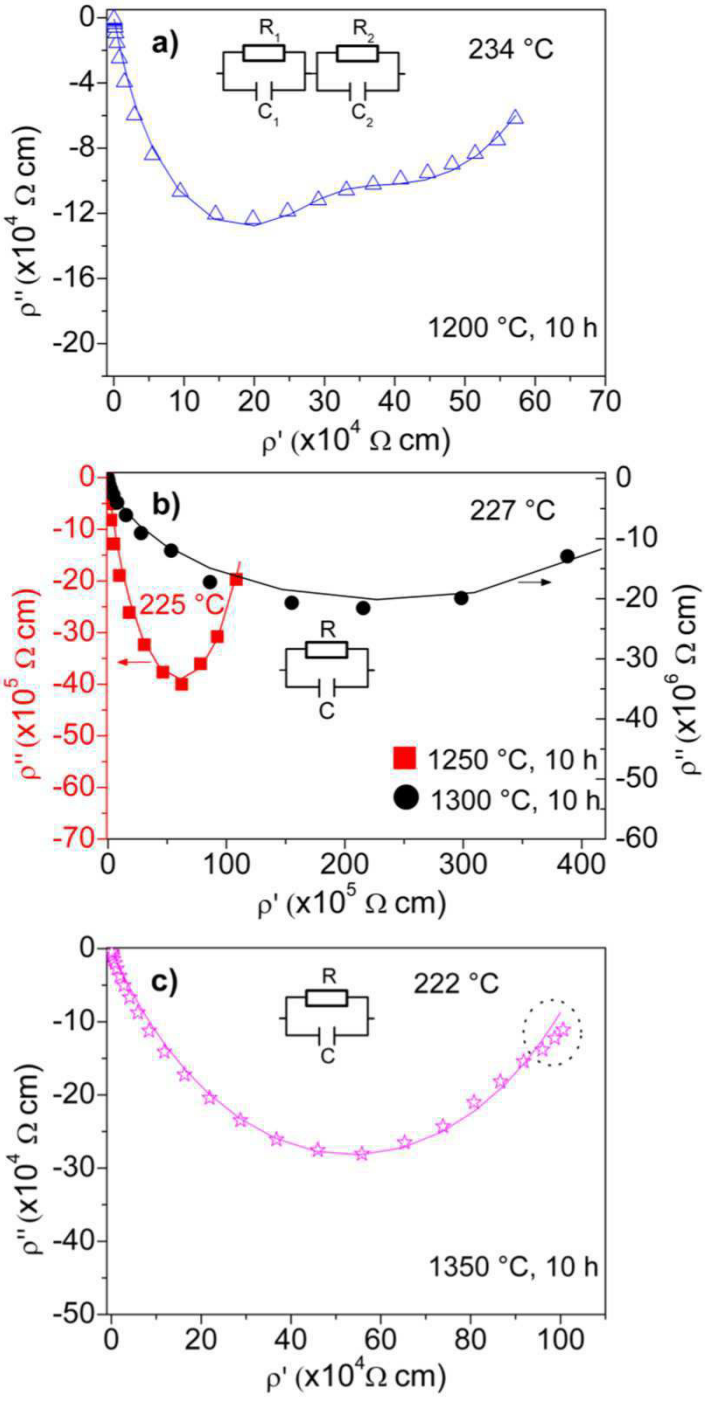

Fig. S7: Cole-Cole plots measured at the indicated temperatures of ceramics sintered at different temperatures. Fits were carried out using the shown equivalent circuit. In (c) the dotted circle marks the appearance of a possible second semicircular arc. Lines are the respective fit results, while symbols correspond to experimental data. The uncertainty of the data is smaller than the symbol size and is lower than 5 %.